Geophysical Research Letters

RESEARCH LETTER
10.1029/2024GL109712

Key Points:

- The wave rose concept is introduced to describe the wavelength directional distribution of TC induced swells with observations far from TCs
- Different observation networks (buoys and satellites) are found to be consistent and complementary to describe this directional distribution
- This directional distribution is characterized during TC Larry life cycle, opening perspectives to improve TC waves parametric models

Supporting Information:

Supporting Information may be found in the online version of this article.

Correspondence to:

C. Pouplin,
clement.pouplin@france-energies-marines.org

Citation:

Pouplin, C., Mouche, A., & Chapron, B. (2024). A multi-sensor approach for the characterization of tropical cyclone induced swell—Application to TC Larry, 2021. *Geophysical Research Letters*, *51*, e2024GL109712. https://doi.org/10.1029/2024GL109712

Received 30 MAY 2024
Accepted 15 SEP 2024

A Multi-Sensor Approach for the Characterization of Tropical Cyclone Induced Swell—Application to TC Larry, 2021

Clément Pouplin[1], Alexis Mouche[2], and Bertrand Chapron[2]

[1]France Energies Marines, Plouzané, France, [2]Institut Francais de Recherche pour l'Exploitation de la Mer (IFREMER), Plouzane, France

Abstract Sea states are likely highly complex and variable under tropical cyclone (TC) conditions. Outrunning the inner core TC vortex, swell systems can radiate in different directions with different wavelengths. Jointly using several sources of wave observations, it is demonstrated that directional properties of wave fields induced by a TC can now be very well recovered. Directional wave information extracted from Sentinel-1 wave mode and CFOSAT SWIM are combined with Sofar Spotter drifters and NDBC buoy network. Specific filtering is applied to deal with respective limitations of these observation systems. High consistency between the different data sources is generally obtained, to provide evolving directional distributions of radiating swell systems during the whole TC life time. TC wave properties can then trace particular events associated to extended fetch effects, quantifying the asymmetrical directional wavelength distributions, as function of the TC main characteristics evolving with time (intensity, size, translation).

Plain Language Summary Strong winds varying at relatively small scale inside tropical cyclones make wave generation processes complex and not properly understood. To improve their performances, wave numerical models can be calibrated using in situ or remote wave data measured inside cyclones. Satellite altimeters can be used to provide wave height data, but wave direction and wavelength satellite observations are still very rare and their quality often hampered by strong winds and heavy rains. Wave buoys provide more reliable data but rarely cross the trajectory of a cyclone. Considering the propagation properties of ocean surface waves, a method is proposed to characterize tropical cyclone induced waves by identifying them far enough from their source, where data are expected to be more accurate and more numerous. Taking advantage of four different platforms (satellites and buoys), it is demonstrated that the properties of waves emitted in almost all directions can now be robustly described during a whole tropical cyclone life cycle.

1. Introduction

Inside tropical cyclones (TCs) intense inner cores, surface wave growth and propagation processes are certainly complex, with transfers of energy toward low frequencies, largely dominated by nonlinear wave-wave interactions. Waves become more organized, longer and directional, to finally outrun their generating strong wind areas. TC translation makes the induced wave field more asymmetrical than its generating wind field. The TC size, wind field distribution and associated large directional gradients, can further enhance these resulting wave field asymmetries (Kudryavtsev et al., 2015; Tannehill, 1937; I. R. Young, 1988; I. Young & Vinoth, 2013). Away from a TC core, nonlinear interactions become negligible, and long-period swells can propagate over large distances (Munk et al., 1963; Snodgrass et al., 1966), radiating a large amount of momentum and energy across ocean basins.

Remote sensing wave measurements inside storms may be significantly hampered (e.g., heavy precipitations and/or imperfect retrieval algorithms), but propagating swells can be measured outside their generation area. Swells are today routinely observed, along coastlines using the Coastal Data Information Program/National Data Buoy Center (CDIP/NDBC, (O'Reilly et al., 2016)), or from space by Synthetic Aperture Radar (SAR) images (Chapron et al., 2001) and Real Aperture Radar measurements (Hauser et al., 2020). Open ocean swell observations are also augmented with a fleet of drifting Sofar Spotter buoys (Houghton et al., 2021). All these observations can be gathered to precisely back-track swells to focal points or source locations, either by utilizing the deep water dispersion relation in spectrograms obtained at a fixed point (Barber & Ursell, 1948; Hell et al., 2019; Munk, 1947; Snodgrass et al., 1966) or by estimating the local convergence of backwards trajectories of wave

groups derived from satellite measurements (Collard et al., 2009; Husson et al., 2012). Note, these techniques have never been applied to TC induced swell systems.

This study aims at characterizing TC induced swell fields considering measurements performed far from the generation area, through a multi-platform approach. After presenting the case study and data, Section 2, the method is briefly outlined in Section 3. The consistency and synergy between the different data sources, in situ (moored and drifting buoys) and satellite (Sentinel-1 SAR and CFOSAT RAR), are illustrated in Section 4. In Section 5, the evolving asymmetrical wave properties emanating from TC Larry are discussed through comparisons with models and related to the TC main characteristics (intensity, size, translation) during its life cycle.

2. Data and Case Study

Wave measurements are referenced with time and location of acquisition and described through three integrated parameters: peak wavelength, peak direction and significant wave height. Buoy networks (Sofar Spotter drifting buoys and NDBC moored buoys) and satellite data sources (Sentinel-1 Level-2 Wave mode and CFOSAT SWIM Level-2S) are considered. Platforms and associated products are detailed in Supporting Information S1 (Text S1.1). TC tracks are taken from the IBTrACS database (Knapp et al., 2010) (Text S1.2 in Supporting Information S1). WAVEWATCH-III ®(WW3) global hindcasts are also used to filter wave data (Text S1.3 in Supporting Information S1).

Selected as a test case for this study, TC Larry started on August 30th, 2021, near the African West coast and crossed the Atlantic ocean, reaching North-East of the Caribbeans before turning Northwards. TC Larry presents several advantages to illustrate the potential of the proposed approach. Its track remains far from the American East coast to capture wave data radiating in every directions, during its whole lifetime. A large amount of Spotter drifters are available during its life cycle, especially above 30° latitude. Also, TC Larry is the only significant extreme event in the Northern Atlantic ocean during its lifetime. Waves originating from another storm and possibly crossing the TC track are unlikely. Finally, TC Larry vitals evolution can be separated into three distinct phases, presented on Figure 1, possibly associated with specific wave field patterns.

- Intensification phase (2021/09/01–2021/09/03): the maximum wind speed increases and the radius of maximum winds decreases.
- Mature phase (2021/09/04–2021/09/07): the maximum wind speed reaches a plateau, while the radius of maximum winds increases.
- Decreasing phase (2021/09/08–2021/09/11): the cyclone accelerates Northwards and becomes an extra-tropical storm, the maximum wind speed decreases and the radius of maximum winds increases.

3. Methodology

All observations of TC induced swell systems are collected by the multi-sensor network and associated to their generation time and location by the TC, through a four steps algorithm.

1. *Pre-filtering unit*: Corresponding almost always to outliers, very high wavelength partitions (>600 m) are discarded. For CFOSAT SWIM estimates, and Sentinel-1 measurements if necessary, the 180° wave direction ambiguity is resolved using WW3 model hindcast (cf. Text S1.3 in Supporting Information S1).
2. *Propagation unit*: Propagation in deep water, without surface currents is assumed. The detected peak wavelength (or peak period for buoy data) solely constrains the peak group velocity of the wave systems. The direction of propagation at measurement location provides the wave group past trajectory along a great circle.
3. *Dynamical co-location unit*: Following the past trajectory of each swell system during 10 days, their location and time of generation are determined by the intersection between the swell trajectory and the TC outer 34 kts wind radius. This criterion is chosen arbitrarily to represent the area generating swell able to propagate far enough from the source to be captured by buoys and satellites. This allows to adapt the co-location area to the TC intensity.
4. *Post-processing unit*: Wave systems are compared to WW3 hindcast at location and time of measurements (using a spectral distance defined in Text S1.3 in Supporting Information S1) to eliminate spurious observations and swell systems that have likely been generated by another storm event.

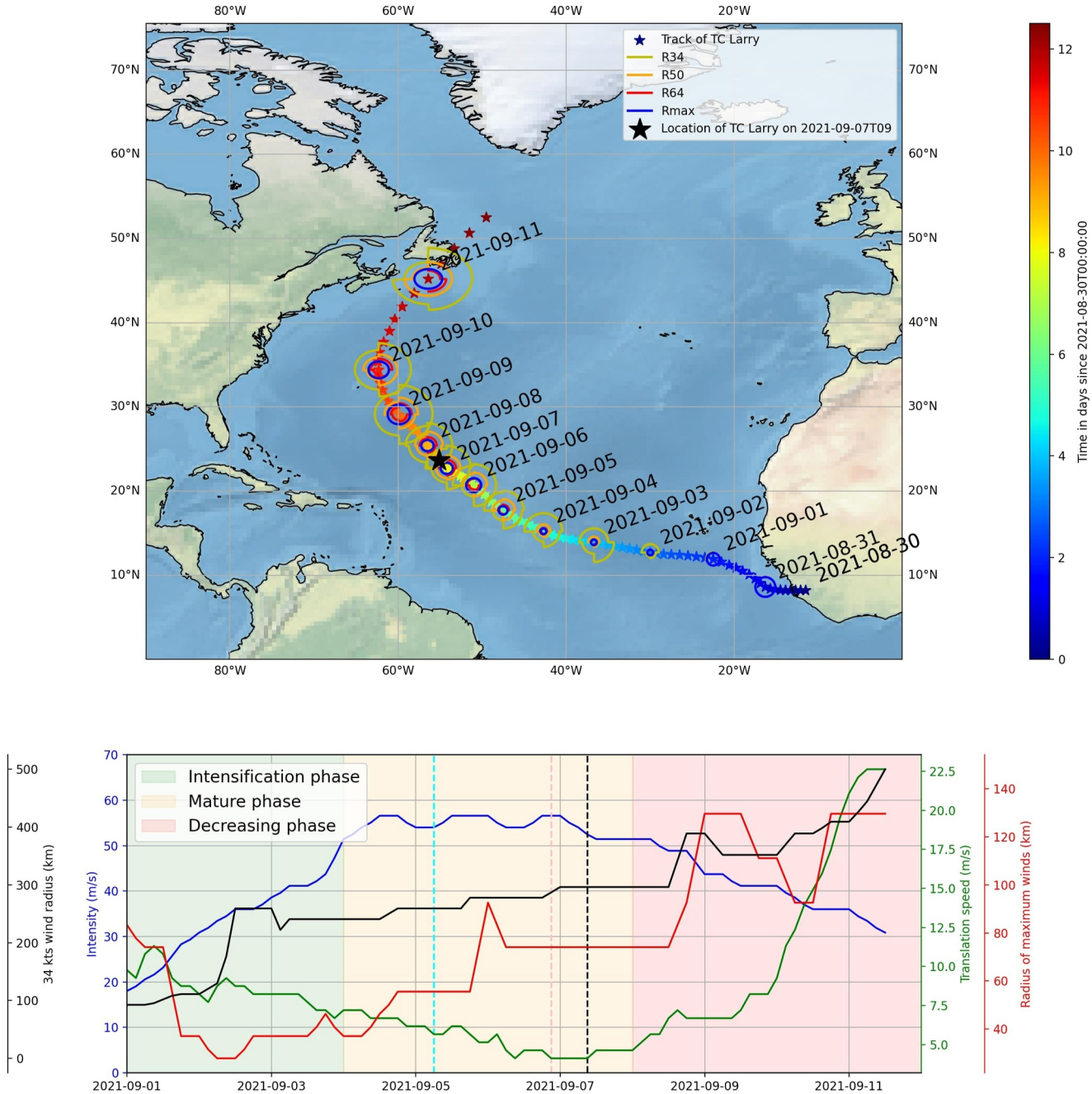

Figure 1. (top) TC track, wind radii are represented by quadrant, every day. (bottom) TC Larry vitals as function of time. The dashed black vertical line corresponds to 09/07 at 9 a.m., the timestamp examined in Section 4. TC location at this timestamp is provided by the black star on the map.

The selected data, identified as swell systems generated by the TC, are gathered in a so-called multi-sensor TC-waves data set. This data set ranges between 2015 and 2023, which corresponds to Sentinel-1 era. A sample corresponding to TC Larry (called observations and propagation data set) is available at https://doi.org/10.17882/99737 (Pouplin et al., 2024). Variables are described in Text S8 in Supporting Information S1.

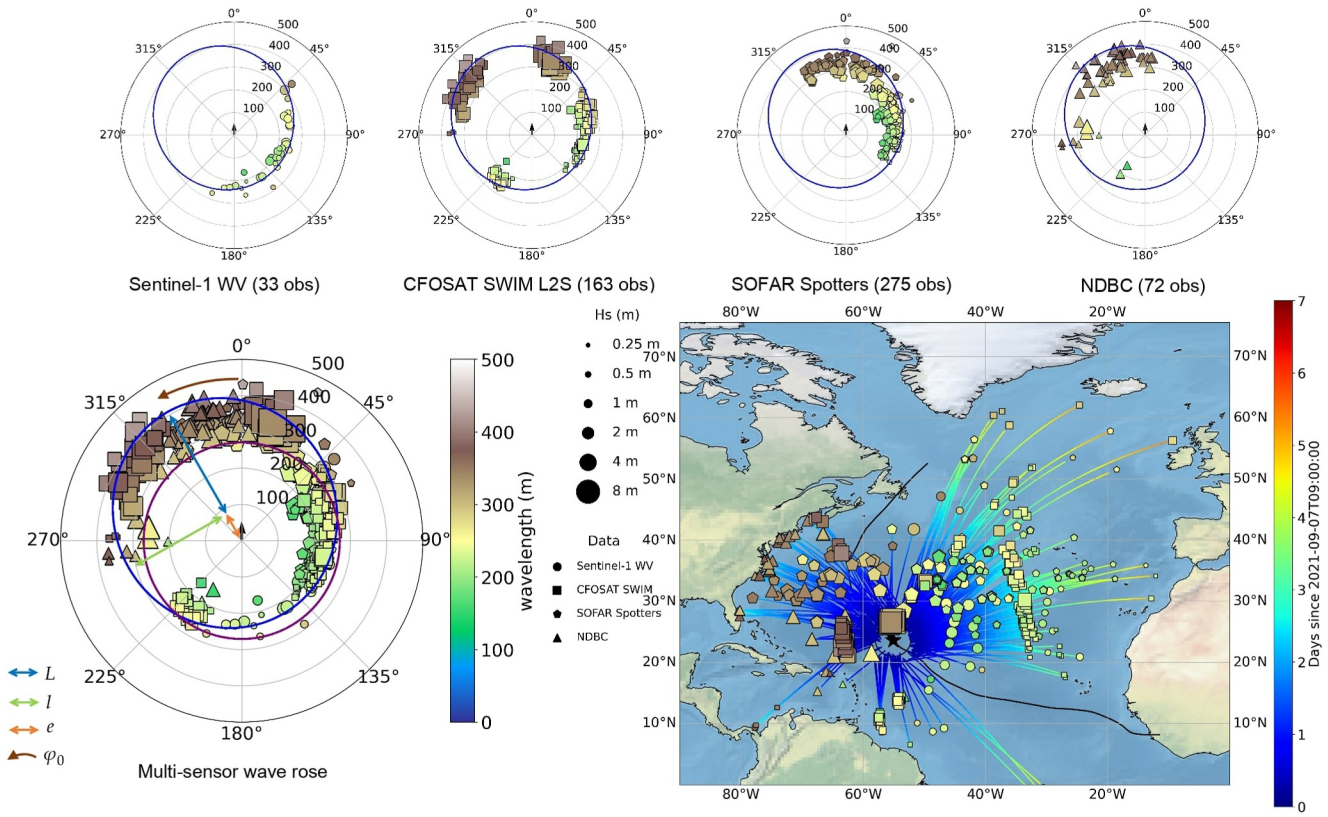

Figure 2. Wavelength directional distribution for TC Larry on 09/07 at 9 a.m. (top) Wave rose for each of four sensors (Bottom left) multi-sensor wave rose. (Bottom right) Map of measurement locations (dots) and TC track (black line).

4. Analysis of the Directional Wavelength Distribution

4.1. The TC Wave Rose Approach

In absence of surface currents, linear swell systems, propagating in deep water, decay in energy but conserve their initial wavelength. The peak wavelength of a swell system acquired along its propagation path is thus not expected to depend on the distance to the source. On Figure 2, results are presented for the wave field generated by TC Larry on 09/07 at 9 a.m., at the end of its mature phase. All measurements of swells that left the TC at this timestamp, and propagating up to 7 days after, are considered.

On the map, wave systems generated at this selected timestamp by the intense wind area (delimited by the 34 knots wind radius, the black circle around TC location represented by the black star) are well captured at latter times and far away from the source. Observations appear spatially scattered and more or less far from the intense wind area. The marker shape, size and color depend on the sensor used, the estimated significant wave height and wavelength, respectively. Back propagation trajectories from the measurement locations to the TC area are color coded, representing the time elapsed since the waves genesis (09/07 at 9 a.m.). The overall resulting directional distribution of the wavelengths generated by the TC is represented in a "wave rose" diagram, where the radius corresponds to the peak wavelength, and the angle gives the direction of propagation of waves from the TC heading. The four wave roses obtained by each sensor individually are displayed on the top row. Each sensor may only cover a fraction of the directional distribution. Sentinel-1 data catch waves propagating toward the left and the rear, Spotter buoys toward the front and the left, and NDBC buoys, mainly located near the American East coast, toward the front and the right. Hindered by the Southern Caribbean islands, the directional sector between 225° and 270° is not covered. This method is thus sensitive to the TC location with respect to buoy networks and to the distance between the TC and the coast, that directly drives the amount of satellite measurements that can be performed along the propagation path of a wave train.

On 09/07 at 9 a.m., the resulting wave rose is still quite complete, and the contributions from the different sensors well overlap on the multi-sensor wave rose. It implies an overall high consistency between the different data sources. It highlights how complementary different platforms can be, especially drifting and moored buoy networks.

4.2. Reduction

From Figure 2, the directional distribution of the wavelengths presents a clear asymmetry. The longest waves (400 m), captured by NDBC and Spotter buoys, and satellite CFOSAT SWIM measurements, are emitted toward the angular sector between 290° and 15° clockwise from the TC direction. Emitted toward the rear sector, up to 250 m long waves are sampled by Sentinel-1 and SWIM measurements. For specific directional sectors, systems with different wavelengths co-exist (this is discussed in Section 5.2). The wavelength difference between waves emitted toward the front and the rear is due to an extended fetch effect, also termed trapped fetch, or group velocity quasi resonance (e.g., Bowyer & MacAfee, 2005; Dysthe & Harbitz, 1987; King & Shemdin, 1978; Kudryavtsev et al., 2015; I. R. Young, 1988; I. Young & Vinoth, 2013). Waves propagating in the same direction than the TC during their generation experiment a longer fetch and reach a longer wavelength than waves leaving the TC by its rear. To quantify this wavelength asymmetry, we consider the maximum wavelength emitted in each direction. For each 10° directional bin, the 90% percentile of measured wavelengths is selected to represent the longest waves. The resulting contour of the wave rose looks elliptical and is reduced with a 4-parameter ellipse, determining the half major axis L, the half minor axis l, the distance to wave rose center e, and the mean orientation ϕ_0 (as defined on Figure 2). The resulting ellipse (blue) and associated four parameters are illustrated on Figure 2. From these parameters, three variables are derived to describe wave field properties.

- The average emitted wavelength $\lambda_0 = \frac{L+l}{2}$, to characterize the integrated wave energy generated by the cyclone.
- The wave rose orientation ϕ_0, the direction toward which the longest waves are mostly emitted.
- The front-rear asymmetry factor $\frac{L+e}{L-e}$, the ratio between the longest and shortest waves emitted by the TC.

To note, extended wave roses (superimposition of a given wave rose with wave roses 3 hr before and after) are considered to perform the reduction procedure. Details are given in Text S3 in Supporting Information S1. These reduced wave properties, such as corresponding IBTrACS wind field parameters, are provided as function of time for TC Larry (life_cycle dataset) https://doi.org/10.17882/99737 (Pouplin et al., 2024). Variables are described in Text S8 in Supporting Information S1.

5. Discussion

5.1. The Wave Rose Asymmetry: Extended Fetch Signature

On 09/07 at 9 a.m., the longest waves generated by the TC propagate toward the front left: $L + e = 409$ m, while the shortest ones propagate toward the rear right: $L - e = 231$ m. 1-D self-similar wave growth models of a translating cyclone, for example, (Kudryavtsev et al., 2015; I. Young & Vinoth, 2013), provide first guess estimates of the longest waves from TC vitals (V_{max}, V_t, R_{max}), by estimating the extended fetch. Model expressions are detailed in Texts S6 and S7 in Supporting Information S1. On 09/07 at 9 a.m., maximum wind, radius of maximum winds and translation speed from the IBTrACS database are $V_{max} = 52.5$ m/s, $R_{max} = 74.1$ km and $V_t = 4.1$ m/s. Both extended fetch models provide similar estimates for the longest waves: 337 and 332 m, respectively. While consistent, both values are largely underestimated compared to observations. Considering a 2D Lagrangian formulation (Kudryavtsev et al., 2021a), self similar solutions (Kudryavtsev et al., 2021b) are also tested. Same conclusions hold, this time for the entire wave rose distribution. Predicted wavelengths are all underestimated. Active downshifts associated to non-linear wave-wave interactions and spectral dispersion of the TC emitted swell trains (discussed in Section 5.2) could explain these differences. The average emitted wavelength (λ_0) escaping the TC is compared to the longest waves that would be emitted by a TC with same vitals but stationary ($V_t = 0$). Following Yurovskaya et al. (2023), this so-called "longest stationary wavelength" (λ_{stat}) is:

$$\lambda_{stat} = \frac{u(r)^2}{g} 2\pi c_a{}^{-2} \left(\frac{rg}{u(r)^2}\right)^{-2q} \quad (1)$$

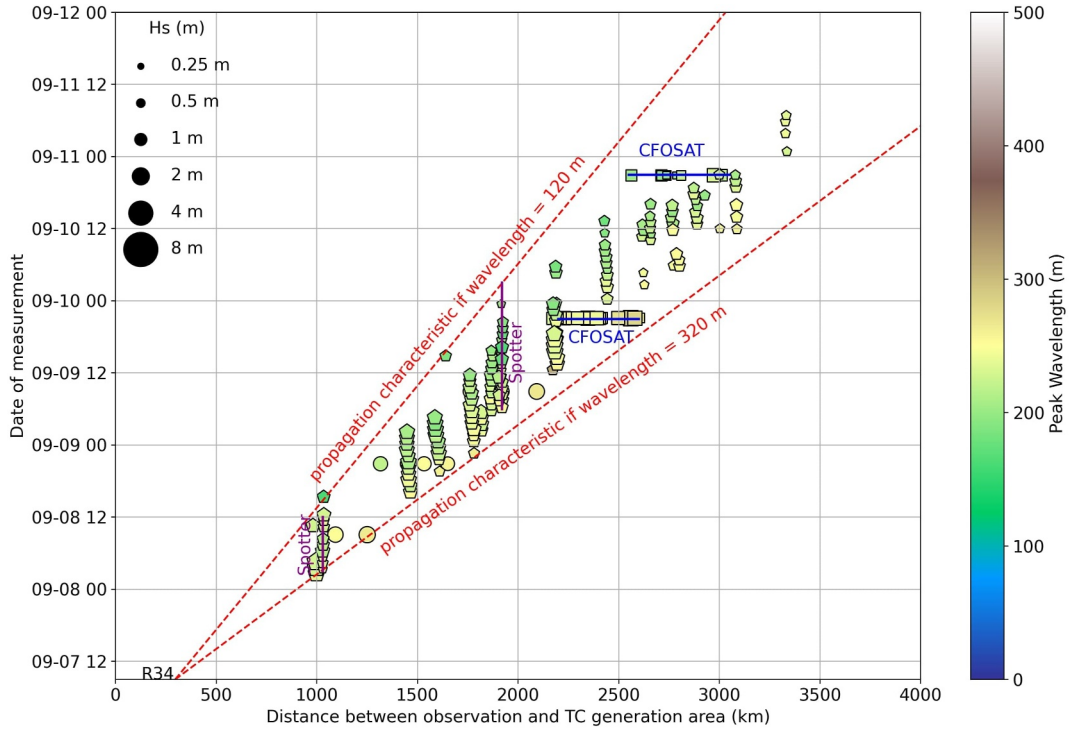

Figure 3. Date of measurement of wave systems generated by Larry on 09/07 at 9 a.m., propagating toward 70° and 85° clockwise from TC direction, as function of distance between TC and measurement locations. Legend for color, size and markers of dots is the same than for Figure 2. Two purple vertical lines and two blue horizontal lines, respectively correspond to time series of acquisitions performed by Spotter buoys and CFOSAT passes.

Where $u(r)$ is the wind speed at distance r from TC center, $c_a = 11.5$, $q = -0.27$, $g = 9.81$. We assume that the longest waves are generated by the highest winds, around $r = R_{\max}$, $u(r) = V_{\max}$. On the multi-sensor wave rose (bottom left on Figure 2), a circle of radius λ_{stat} is reported in purple. λ_{stat} (271 m) is slightly smaller than λ_0 (313 m). On this example, λ_{stat} is closer to the wavelength emitted toward the rear than toward the front. This is further discussed in Section 5.3.

5.2. Wave Rose Radial Thickness

The merged wave rose is quite thick radially within a given angular sector. Leaving the TC active wind regions and propagating almost freely in open ocean, the originating wave system may be characterized by an initial broad wavenumber spectral bandwidth. Following linear dispersion, longer waves propagate faster than shorter ones, and an initially continuous spectral distribution progressively spreads along the spatial domain. Far enough from the TC, wavenumber components become sufficiently separated to be easily distinguished. Both in situ and satellite measurements trace this wave dispersion effect in their data records in two different ways (Figure 3):

- A buoy, whose drifting speed is null (mooring) or much smaller (drifting) than wave trains group velocity, records wave systems in the time domain, successively receiving the energy associated to each frequency component of the initial wave system (vertical purple lines on Figure 3).
- A satellite pass provides measurements at several locations, considered to all occur at the same time. Information on the initial wave spectral distribution can also be traced: the shortest (longest) waves are likely the closest (farthest) from their initial common source (horizontal blue lines on Figure 3).

On Figure 3, wave systems propagating within the directional sector 70° and 85° clockwise to the TC direction (delimited by green dotted lines on Figure S6 in Supporting Information S1) are distributed with distance traveled and time elapsed between their estimated generating area and measurement locations. All observations are contained in a cone delimited by the red dotted lines, corresponding to wave groups characteristics with wavelengths between 120 and 320 m, respectively. Several Spotter buoys retrieve the progressive arrival of TC Larry's

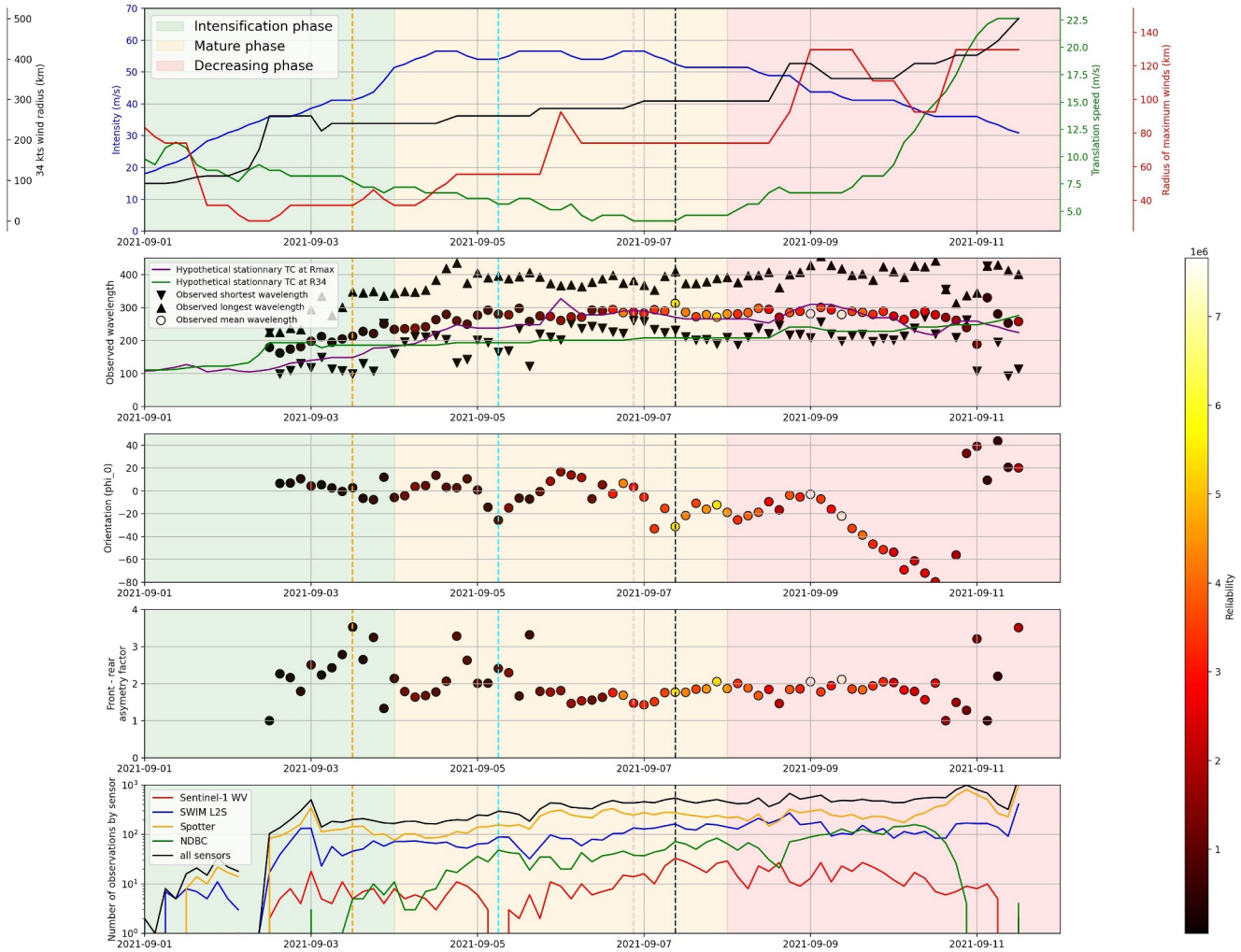

Figure 4. Evolution of wave rose characteristics as function of time, the dotted vertical line corresponds to particular timestamps. In black, 09/07 at 9 a.m., examined on Figure 2 as a wave rose example. In orange, cyan and pink respectively, 09/03 at 12 p.m., 09/05 at 6 a.m. and 09/06 at 9 p.m., that are analysed in Text S5 in Supporting Information S1.

wave trains along the propagation path. Located at 1,000 km, a buoy catches a wave train for approximately 12 hr. At about 1,900 km from TC Larry, buoys record waves during 18–24 hr, illustrating the increasing spatial spread of the initial wave system further away from the source (Collard et al., 2009; Delpey et al., 2010). More rapidly dissipated during their propagation, few short waves (<200 m) are acquired further than 2,500 km from the source.

To note, the initial spectral bandwidth broadness may largely be associated to the complexity of the wind field within the TC inner core. Superimposed, wave systems with different wavelengths and directions are likely to occur. Wave systems propagating toward the same direction but with different wavelengths can also co-exist. This is tested and discussed in Text S4 in Supporting Information S1 using a parametric wave model (Kudryavtsev et al., 2021a).

5.3. Dynamical Evolution of Wavelength Directional Distribution

Wave roses and derived wave field characteristics are regularly obtained and analyzed along the whole TC life-cycle to examine the influence of the TC main characteristics (vortex intensity, translation speed, wind radii). TC Larry vitals with respect to time are presented on Figure 4 (top panel). For each timestamp, the elliptical reduction (Section 4.2) is performed with an associated reliability value, related to the wave rose directional filling and the error on the elliptical fit (details and time series of error are given in Text S2 in Supporting Information S1). The

three observed wave field characteristics over the whole TC lifetime are presented on Figure 4. The most reliable fits are obtained between 09/07 and 09/10, corresponding to the end of the mature phase, and beginning of the decreasing phase. The number of observations for each sensor is presented on the bottom panel.

Figure 4 also displays the mean emitted wavelength, the longest ($L + e$) and shortest ($L - e$) emitted waves, on the second panel. Occasionally, observed shortest waves are longer than the mean wavelength. Such situations are rare, usually related to wrong fits, but happen for example, on 09/02 at 12 p.m., during the very beginning of the TC life cycle, when the 34 knots wind radius is small compared to the mature phase (less than 200 km). Smaller R_{34} values reduce the chance of intersection with wave system trajectories. Weak winds generate shorter waves which dissipate faster than longer ones, and could only be acquired at relatively small distances from their generation area. Wave data are lacking at these early times, making elliptical fits less reliable than during the mature phase.

The mean emitted wavelength increases until 09/05 to reach 300 m, approximately. This increase takes place during the TC intensification phase. While parameters V_{max}, R_{max} and V_t continue to vary, the mean wavelength stabilizes around 300 m, from 09/05 until the end of the TC lifetime. Such a directional average of emitted wavelength can be compared to the theoretical stationary wavelength λ_{stat} (Equation 1). This wavelength is computed at different distances from the TC center, using different couples (r, $u(r)$) along the wind speed profile. Based on the wind radii time series provided by IBTrACS (34, 50, 64 knots and radius of maximum winds), our analysis shows that the stationary wavelength is the longest when forced around the radius of maximum winds (purple curve), except at the very beginning of the TC life cycle (the green curve representing waves forced at R_{34}). λ_{stat} is always slightly smaller but correlated to the observed mean wavelength, as already suggested in Section 4.2 for a particular timestamp. Given reliable TC vitals, the mean wavelength can thus be quite robustly estimated. It seems that the mean wavelength is estimated more accurately by λ_{stat} when the front rear asymmetry is small enough.

The wave rose orientation (ϕ_0), strongly varies in time as it is very sensitive to small variations of samples in each wave rose. Before 09/05, average ϕ_0 stays around 0°, but the reliability of the fit is quite low. In this phase, TC Larry is traveling quite rapidly (≥7 m/s), with increasing maximum wind speeds (between 20 and 50 m/s). In such conditions, the longest waves are found to propagate in the same direction than the cyclone ($\phi_0 = 0$) and are seemingly not impacted by the cyclonic wind gradients. On 09/05 at 6 a.m., the longest wavelengths keep being emitted toward 0° but the shortest wavelength is reported to be emitted in the right rear quadrant, thus slightly offsetting the wave rose orientation counterclockwise, and making ϕ_0 decrease to −25°. More details are available in Text S5 in Supporting Information S1. Still, the longest wavelengths are found around 0° until 09/07. More systematically, ϕ_0 decreases to −20° between 09/07 and 09/08. During this phase the cyclone is moving relatively slowly compared to the intensification phase (≤5 m/s). The maximum wind speed (≥50 m/s) is likely sufficient to rotate the longest wave groups experiencing extended fetch toward the left hand side of the TC when they reach the right front quadrant. The bell-shape pattern between 09/08 and 09/10 at 12 p.m. is related to two consecutive effects. First the cyclone accelerates (from 5 to 7 m/s) and the waves cannot be bent any longer by front-right quadrant winds (increase of ϕ_0 until 09/09). The cyclone acceleration continues and is combined with a sudden change of the TC heading direction from North-West to North-East. It significantly impacts the reference direction used to compute ϕ_0, causing the decrease of ϕ_0 until 09/10 at 12 p.m.

Before 09/06, the front rear asymmetry $\frac{L+e}{L-e}$ (presented on fourth panel) is large and erratic. At strongest asymmetry, short waves (100 m approximately) are generated toward the rear, compared to almost 350 m long trapped waves toward the front, to give a factor of 3.5 (see the wave rose on 09/03 at 12 p.m. on Figure S8 in Text S5 in Supporting Information S1). Transitioning to the mature phase, the front-rear asymmetry factor reduces and stabilizes between 1.5 and 2 until 09/10.

6. Conclusion

A methodology is developed to combine multi-sensor capabilities and more precisely describe swell fields generated by TCs, taking advantage of data observed far from the generation area. The TC wave rose representation is introduced to synthesize the directional distribution of wavelengths emitted by the TC, and demonstrate the synergy and consistency between the different data sources, in the case of TC Larry. This

representation can be reduced to four parameters to document wave field characteristics (mean wavelength, direction of longest waves, front-rear asymmetry).

Along a TC life cycle, wave roses and associated parameters provide observational evidences of TC extended fetch effects. Reported longest wavelengths are found, at time, much larger than modeled ones. Simplified parametric models may not be able to catch the whole spatial-temporal complexity of TC wind fields and non-linear wave-wave interactions. Within the cyclone inner core, intense swirling winds generate waves in different directions and under different fetches. Wave packets propagating at different group velocities can experience focusing effects, locally enhancing wave steepness, and thus non-linear wave-wave wavelength upshift effects. Far from the active TC wind regions, linear wave dispersion applies. Wave trains spread along their trajectories, and can be individually distinguished at a given buoy location. Building on the demonstrated potential to effectively merge in situ and satellite measurements, the present study thus opens new means to help calibrate parametric models and better identify these intense upshift wavelength effects.

The present methodology will further be improved by combining other wave measurements, foremost standard altimeter sea state estimates, but also new available larger swath SAR and SWOT for significant wave height estimates and forerunners detection. Also considering the rapid development of wave buoy devices and networks, including drifting buoys, saildrones and wave gliders, the TC wave rose methodology will be extended to include significant wave height estimates and further characterize the wave energy and its dissipation as function of direction of propagation, through a data-driven approach. Performed over growing TC data bases, these future investigations could provide new capabilities to derive robust and immediate first-guess estimates for the directional energy distribution of swell systems generated by TCs, as function of their main wind field parameters (V_{max}, R_{max}, V_t, inflow, asymmetry and sharpness of the wind profile). Correlations between the wind and wave asymmetries could be investigated (Zhang et al., 2016, 2020, 2021).

Data Availability Statement

The two processed data sets mentioned in the text (observations in Section 3 and life cycle in Section 4.2) and an associated jupyter notebook are available (Pouplin et al., 2024).

Acknowledgments
This study was funded by ESA MAXSS (4000132954/20/I-NB) and FEM OROWSHI projects. Thanks to SOFAR Ocean for providing the Spotter buoys data.

References

Barber, N. F., & Ursell, F. (1948). The generation and propagation of ocean waves and swell. I. wave periods and velocities. *Philosophical Transactions of the Royal Society of London - Series A: Mathematical and Physical Sciences*, *240*(824), 527–560.

Bowyer, P. J., & MacAfee, A. W. (2005). The theory of trapped-fetch waves with tropical cyclones—An operational perspective. *Weather and Forecasting*, *20*(3), 229–244. https://doi.org/10.1175/WAF849.1

Chapron, B., Johnsen, H., & Garello, R. (2001). Wave and wind retrieval from SAR images of the ocean. *Annales des Telecommunications*, *56*(11–12), 682–699. https://doi.org/10.1007/bf02995562

Collard, F., Ardhuin, F., & Chapron, B. (2009). Monitoring and analysis of ocean swell fields from space: New methods for routine observations. *Journal of Geophysical Research*, *114*(C7), C07023. https://doi.org/10.1029/2008jc005215

Delpey, M. T., Ardhuin, F., Collard, F., & Chapron, B. (2010). Space-time structure of long ocean swell fields. *Journal of Geophysical Research*, *115*(C12), C12037. https://doi.org/10.1029/2009jc005885

Dysthe, K., & Harbitz, A. (1987). Big waves from polar lows? *Tellus*, *39*(5), 500–508. https://doi.org/10.1111/j.1600-0870.1987.tb00324.x

Hauser, D., Tourain, C., Hermozo, L., Alraddawi, D., Aouf, L., Chapron, B., et al. (2020). New observations from the SWIM radar on-board CFOSAT: Instrument validation and ocean wave measurement assessment. *IEEE Transactions on Geoscience and Remote Sensing*, *59*(1), 5–26. https://doi.org/10.1109/tgrs.2020.2994372

Hell, M. C., Cornelle, B. D., Gille, S. T., Miller, A. J., & Bromirski, P. D. (2019). Identifying ocean swell generation events from ross ice shelf seismic data. *Journal of Atmospheric and Oceanic Technology*, *36*(11), 2171–2189. https://doi.org/10.1175/jtech-d-19-0093.1

Houghton, I., Smit, P., Clark, D., Dunning, C., Fisher, A., Nidzieko, N., et al. (2021). Performance statistics of a real-time Pacific Ocean weather sensor network. *Journal of Atmospheric and Oceanic Technology*, *38*(5), 1047–1058. https://doi.org/10.1175/jtech-d-20-0187.1

Husson, R., Ardhuin, F., Collard, F., Chapron, B., & Balanche, A. (2012). Revealing forerunners on Envisat's wave mode ASAR using the global seismic network: Forerunners seen by SAR and seismic noise. *Geophysical Research Letters*, *39*(15), L15609. https://doi.org/10.1029/2012GL052334

King, D., & Shemdin, O. (1978). Radar observation of hurricane wave directions. In *Coastal engineering 1978* (pp. 209–226). Coastal Engineering.

Knapp, K. R., Kruk, M. C., Levinson, D. H., Diamond, H. J., & Neumann, C. J. (2010). The international best track archive for climate stewardship (IBTRACS): Unifying tropical cyclone data. *Bulletin of the American Meteorological Society*, *91*(3), 363–376. https://doi.org/10.1175/2009BAMS2755.1

Kudryavtsev, V., Golubkin, P., & Chapron, B. (2015). A simplified wave enhancement criterion for moving extreme events. *Journal of Geophysical Research: Oceans*, *120*(11), 7538–7558. https://doi.org/10.1002/2015JC011284

Kudryavtsev, V., Yurovskaya, M., & Chapron, B. (2021a). 2D parametric model for surface wave development under varying wind field in space and time. *Journal of Geophysical Research: Oceans*, *126*(4), e2020JC016915. https://doi.org/10.1029/2020JC016915

Kudryavtsev, V., Yurovskaya, M., & Chapron, B. (2021b). Self-similarity of surface wave developments under tropical cyclones. *Journal of Geophysical Research: Oceans*, *126*(4), e2020JC016916. https://doi.org/10.1029/2020JC016916

Munk, W. H. (1947). Tracking storms by forerunners of swell. *Journal of the Atmospheric Sciences*, *4*(2), 45–57. https://doi.org/10.1175/1520-0469(1947)004<0045:tsbfos>2.0.co;2

Munk, W. H., Miller, G., Snodgrass, F., & Barber, N. F. (1963). Directional recording of swell from distant storms. *Philosophical Transactions of the Royal Society of London - Series A: Mathematical and Physical Sciences*, *255*(1062), 505–584.

O'Reilly, W. C., Olfe, C. B., Thomas, J., Seymour, R., & Guza, R. (2016). The California coastal wave monitoring and prediction system. *Coastal Engineering*, *116*, 118–132. https://doi.org/10.1016/j.coastaleng.2016.06.005

Pouplin, C., Mouche, A., & Chapron, B. (2024). Characterisation of the wave field induced by tropical cyclone Larry from a multi-sensor approach [Dataset]. *SEANOE*. https://doi.org/10.17882/99737

Snodgrass, F., Hasselmann, K., Miller, G., Munk, W. H., & Powers, W. (1966). Propagation of ocean swell across the pacific. *Philosophical Transactions of the Royal Society of London - Series A: Mathematical and Physical Sciences*, *259*(1103), 431–497.

Tannehill, I. (1937). Sea swells in relation to the movement and intensity of tropical storms. *International Hydrographic Review*.

Young, I., & Vinoth, J. (2013). An "extended fetch" model for the spatial distribution of tropical cyclone wind–waves as observed by altimeter. *Coastal Engineering*, *70*, 14–24. https://doi.org/10.1016/j.oceaneng.2013.05.015

Young, I. R. (1988). Parametric hurricane wave prediction model. *Journal of Waterway, Port, Coastal, and Ocean Engineering*, *114*(5), 637–652. https://doi.org/10.1061/(asce)0733-950x(1988)114:5(637)

Yurovskaya, M., Kudryavtsev, V., & Chapron, B. (2023). A self-similar description of the wave fields generated by tropical cyclones. *Ocean Modelling*, *183*, 102184. https://doi.org/10.1016/j.ocemod.2023.102184

Zhang, G., Li, X., Perrie, W., & Zhang, J. A. (2021). Tropical cyclone winds and inflow angle asymmetry from SAR imagery. *Geophysical Research Letters*, *48*(20), e2021GL095699. https://doi.org/10.1029/2021gl095699

Zhang, G., Perrie, W., Li, X., & Zhang, J. A. (2016). A hurricane morphology and sea surface wind vector estimation model based on c-band cross-polarization SAR imagery. *IEEE Transactions on Geoscience and Remote Sensing*, *55*(3), 1743–1751. https://doi.org/10.1109/tgrs.2016.2631663

Zhang, G., Perrie, W., Zhang, B., Yang, J., & He, Y. (2020). Monitoring of tropical cyclone structures in ten years of Radarsat-2 SAR images. *Remote Sensing of Environment*, *236*, 111449. https://doi.org/10.1016/j.rse.2019.111449